

Intelligent Reflecting Surface-Aided SWIPT: Joint Waveform, Active and Passive Beamforming Design

Yang Zhao, *Member, IEEE*, Bruno Clerckx, *Senior Member, IEEE*, and Zhenyuan Feng, *Member, IEEE*

Abstract—The performance of Simultaneous Wireless Information and Power Transfer (SWIPT) is mainly constrained by the received Radio-Frequency (RF) signal strength. To tackle this problem, we introduce an Intelligent Reflecting Surface (IRS) to compensate the propagation loss and boost the transmission efficiency. This paper proposes a novel IRS-aided SWIPT system where a multi-carrier multi-antenna Access Point (AP) transmits information and power simultaneously to a single-antenna User Equipment (UE) under the assist of an IRS. Considering energy harvester nonlinearity and practical transceiving strategies, we characterize the achievable Rate-Energy (R-E) region through a joint design of waveform, active and passive beamforming based on the Channel State Information at the Transmitter (CSIT). This non-convex problem is then solved by the Block Coordinate Descent (BCD) method, where the active precoder is obtained in a closed form, the passive beamformer is optimized by the Successive Convex Approximation (SCA) approach, and the waveform is designed by the Geometric Programming (GP) technique. Since the computational complexity of the GP-based algorithm scales exponentially with the number of subbands, we also propose two low-complexity adaptive waveform design to facilitate practical SWIPT implementation. Simulation results show considerable R-E gain over benchmark schemes and demonstrate the importance of accounting harvester nonlinearity in the passive beamforming design.

Index Terms—Simultaneous wireless information and power transfer, intelligent reflecting surface, waveform design, beamforming design, energy harvester nonlinearity.

I. INTRODUCTION

A. Simultaneous Wireless Information and Power Transfer

WITH the great advance in communication performance, a bottleneck of wireless networks has come to energy supply. Simultaneous Wireless Information and Power Transfer (SWIPT) is a promising solution to connect and power mobile devices via electromagnetic waves in the Radio-Frequency (RF) band. It provides low power at μW level but broad coverage up to hundreds of meters in a sustainable and controllable manner, bringing more opportunities to the Internet of Things (IoT) and Machine to Machine (M2M) networks. The upsurge in the number of wireless devices, together with the decrease of electronics power consumption, calls for a re-thinking of future wireless networks based on Wireless Power Transfer (WPT) and SWIPT [1].

The concept of SWIPT was first cast in [2], where the authors investigated the Rate-Energy (R-E) tradeoff for a flat Gaussian channel and typical discrete channels. [3] proposed

two practical co-localized information and power receivers, i.e. Time Switching (TS) and Power Splitting (PS). Dedicated information and energy beamforming were then investigated in [4], [5] to characterize the R-E region for multi-antenna broadcast and interference channels. On the other hand, [6] pointed out that the RF-to-Direct Current (DC) conversion efficiency of rectifiers depends on the input power and waveform shape. It implies that the modeling of the energy harvester, in particular its nonlinearity, has a crucial and significant impact on the waveform preference, resource allocation and system design of any wireless-powered systems [1], [6], [7]. Motivated by this, [8] derived a tractable nonlinear harvester model based on the Taylor expansion of diode I-V characteristics, then performed joint waveform and beamforming design for WPT. Simulation and experiments showed the benefit of modeling energy harvester nonlinearity in real system design [9], [10] and demonstrated the joint waveform and beamforming strategy as a key technique to expand the operation range [11]. A low-complexity adaptive waveform design by Scaled Matched Filter (SMF) was proposed in [12] to exploit the rectifier nonlinearity, whose advantage is then demonstrated in a prototype with channel acquisition [13]. Beyond WPT, [14] uniquely showed that the rectifier nonlinearity brings radical changes to SWIPT design, namely 1) modulated and unmodulated waveforms are not equally suitable for wireless power delivery, 2) a multi-carrier unmodulated waveform superposed to a multi-carrier modulated waveform can enlarge the R-E region of SWIPT, 3) a combination of PS and TS is generally the best strategy, 4) the optimal input distribution is not the conventional Circularly Symmetric Complex Gaussian (CSCG), 5) the rectifier nonlinearity is beneficial to system performance and is essential to efficient SWIPT design. Those observations, validated experimentally in [9], led to the question: *What is the optimal input distribution for SWIPT under nonlinearity?* This question was answered in [15] for single-carrier SWIPT, and some attempts were further made in [16] for multi-carrier SWIPT. The answer sheds new light to fundamental limits of SWIPT and practical signaling (e.g. modulation and waveform) strategies. It is now well understood from [14]–[16] that, due to the nonlinearity, a combination of CSCG and on-off keying in single-carrier setting and non-zero mean asymmetric inputs in multi-carrier setting lead to significantly larger R-E region compared to conventional CSCG. Recently, [17] used machine learning techniques to design SWIPT signaling under nonlinearity to complement the information-theoretic results of [15], and new modulation schemes were subsequently invented.

The authors are with the Department of Electrical and Electronic Engineering, Imperial College London, London SW7 2AZ, U.K. (e-mail: {yang.zhao18, b.clerckx, zhenyuan.feng19}@imperial.ac.uk).

This paper has been submitted for publication.

B. Intelligent Reflecting Surface

Intelligent Reflecting Surface (IRS) has recently emerged as a promising technique that adapts the propagation environment to enhance the spectrum and energy efficiency. In practice, an IRS consists of multiple individual reflecting elements to adjust the amplitude and phase of the incoming signal for a smart reflection (i.e. passive beamforming). Different from relay, backscatter and Frequency-Selective Surface (FSS) [18], IRS adaptively assists the primary transmission by passive components to suppress thermal noise but is limited to frequency-dependent reflection.

Inspired by the development of real-time reconfigurable metamaterials [19], the authors of [20] introduced a programmable metasurface that steers or polarizes the electromagnetic wave at a specific frequency to mitigate signal attenuation. Motivated by this, [21] proposed an IRS-assisted Multiple-Input Single-Output (MISO) system and jointly optimized the precoder at the Access Point (AP) and the phase shifts at the IRS to minimize the transmit power. The active and passive beamforming problem was then extended to the discrete phase shift case [22] and the multi-user case [23]. In [24], the authors investigated the impact of non-zero resistance on the reflection pattern and emphasized the dependency of the reflection amplitude on the phase shift for practical IRS. To estimate the cascaded AP-IRS-User Equipment (UE) link without RF-chains at the IRS, practical protocols based on element-wise on/off switching [25], reflection pattern design [26], [27], and compressed sensing [28] have been proposed. [29] considered a novel dynamic passive beamforming for Orthogonal Frequency-Division Multiplexing (OFDM) systems, where the reflection coefficient is varied over consequent time slots to enable flexible resource allocation over time-frequency Resource Blocks (RBs). In [30], a prototype IRS with 256 2-bit elements based on Positive Intrinsic-Negative (PIN) diodes was developed to support real-time high-definition video transmission at GHz and mmWave frequency.

C. IRS-Aided SWIPT

Both SWIPT and IRS aim to achieve spectrum and energy efficient transmission, and the effective channel enhancement and low power consumption of IRS are expected to bring more opportunities to SWIPT. For a multi-user IRS-aided SWIPT system, dedicated energy beams are proved unnecessary for the Weighted Sum-Power (WSP) maximization problem [31] but essential when fairness issue is considered [32]. It was also demonstrated in [33] that Line-of-Sight (LoS) links can boost the WSP because rank-deficient channels require less energy beams. However, the above papers only consider single-carrier transmission based on an inaccurate linear energy harvester model. Motivated by this, we marry the benefits of joint multi-carrier waveform and active beamforming optimization for SWIPT (accounting for nonlinearity) with the passive beamforming capability of IRS in this paper. We ask ourselves the important question: *How to jointly exploit the spatial domain and the frequency domain efficiently through joint waveform and beamforming design to enlarge the R-E region of IRS-aided SWIPT?* The contributions of this paper are summarized as follows.

First, we propose a novel IRS-aided SWIPT architecture based on joint waveform, active and passive beamforming design. To elevate the rectifier nonlinearity, we superpose a multi-carrier unmodulated power waveform (deterministic multisine) to a multi-carrier modulated information waveform and evaluate the performance under TS and PS modes. The proposed joint waveform, active and passive beamforming architecture exploits rectifier nonlinearity, beamforming gain and channel selectivity across spatial and frequency domains to enlarge the achievable R-E region. This is the first paper to tackle energy harvester nonlinearity, multi-carrier transmission, and co-localized receiver for IRS-aided SWIPT.

Second, we characterize the achievable R-E region with multiple energy maximization problems with different rate constraints, and solve each R-E boundary point by an Block Coordinate Descent (BCD) algorithm based on the Channel State Information at the Transmitter (CSIT). For active beamforming, we prove that the global optimal active information and power precoders coincide at Maximum-Ratio Transmission (MRT) under rectifier nonlinearity. For passive beamforming, we propose a Successive Convex Approximation (SCA) algorithm that obtains the IRS reflection coefficient by relax-then-extract method. Finally, the superposed waveform is optimized by the Geometric Programming (GP) technique. The IRS phase shift, active precoder and waveform amplitude are updated iteratively until convergence.

Third, we introduce two low-complexity adaptive waveform design in the closed form to avoid the exponential complexity of the GP algorithm. The Water-Filling (WF) strategy for modulated waveform and SMF strategy for multisine waveform are combined under TS and PS setups to facilitate practical SWIPT implementation. To cooperate with the low-complexity waveform schemes, we modify the passive beamforming algorithm and characterize the R-E region by varying the duration ratio for TS and the waveform and splitting ratios for PS. The performance of the low-complexity design is proved close to the BCD algorithm under different configurations.

Fourth, we provide numerical results to evaluate the performance of the proposed algorithms. It is concluded that 1) the proposed BCD algorithm always converge to local optimal points, 2) multisine waveform is beneficial to multi-carrier energy transfer especially when the number of subbands is large, 3) TS is preferred at low Signal-to-Noise Ratio (SNR) while PS is preferred at high SNR, 4) there exist two optimal IRS development locations, one close to the AP and one close to the UE, 5) the output SNR scales linearly with the number of transmit antennas and quadratically with the number of IRS elements, 6) due to rectifier nonlinearity, the output DC current scales quadratically with the number of transmit antennas and quartically with the number of IRS elements, 7) at different R-E points, the optimal IRS reflection coefficients coincide for narrowband SWIPT but differ for broadband SWIPT, 8) the proposed algorithms are robust to practical limitations as inaccurate cascaded CSIT and finite IRS reflection states.

Organization: Section II introduces the system model, transceiving mode and rectifier nonlinearity. Section III formulates the problem and tackles the waveform, active and passive beamforming optimization. Section IV presents the simulation

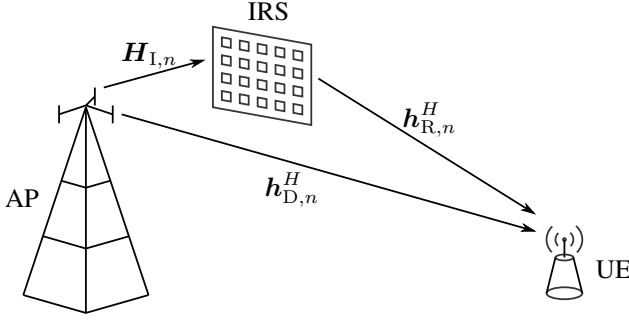


Fig. 1. An IRS-aided multi-carrier SWIPT system.

results and evaluates the proposed algorithms. Section V concludes the paper.

Notations: Scalars, vectors and matrices are denoted respectively by italic, bold lower-case and bold upper-case letters. j denotes the imaginary unit. $\mathbb{C}^{x \times y}$ denotes the subspace spanned by complex $x \times y$ matrices. $\Re\{\cdot\}$ and $\Im\{\cdot\}$ denote respectively the real and imaginary part of a complex entity. $(\cdot)^*$, $(\cdot)^T$, $(\cdot)^H$, $(\cdot)^+$, $|\cdot|$, $\|\cdot\|$ represent respectively the conjugate, transpose, conjugate transpose, ramp function, absolute value, and Euclidean norm operators. $\arg(\cdot)$, $\text{rank}(\cdot)$, $\text{Tr}(\cdot)$, $\text{diag}(\cdot)$ denote the argument, rank, trace, and a square matrix with input elements on the main diagonal. $\mathbf{S} \succeq 0$ means \mathbf{S} is positive semi-definite. $\mathbb{A}\{\cdot\}$ extracts the DC component of a signal. $\mathbb{E}_X\{\cdot\}$ takes expectation with respect to random variable X (X is omitted for simplicity). The distribution of a CSCG random vector with mean $\mathbf{0}$ and covariance $\mathbf{\Sigma}$ is denoted by $\mathcal{CN}(\mathbf{0}, \mathbf{\Sigma})$. \sim means "distributed as". $(\cdot)^*$ and $(\cdot)^{(i)}$ denote respectively the stationary value and the value at iteration i .

II. SYSTEM MODEL

As shown in Fig. 1, we propose an IRS-aided SWIPT system where a M -antenna AP delivers information and power simultaneously, through a L -element IRS, to a single-antenna UE over N orthogonal evenly-spaced subbands. We consider quasi-static block fading and assume the CSIT of AP-UE and AP-IRS-UE cascaded channels are known. The signals reflected by two or more times are omitted and the noise power is assumed too small to be harvested.

A. Transmitted Signal

Denote $\tilde{x}_{I,n} \sim \mathcal{CN}(0, 1)$ as the information symbol transmitted over subband $n \in \{1, \dots, N\}$. The superposed signal transmitted on antenna $m \in \{1, \dots, M\}$ at time t is

$$x_m(t) = \Re \left\{ \sum_{n=1}^N (w_{I,n,m} \tilde{x}_{I,n}(t) + w_{P,n,m}) e^{j2\pi f_n t} \right\} \quad (1)$$

where $w_{I/P,n,m}$ denotes the complex weight of the modulated/multisine waveform transmitted at subband n on antenna m , and f_n is the frequency of subband n . On top of this, we

stack up $\mathbf{w}_{I/P,n} \triangleq [w_{I/P,n,1}, \dots, w_{I/P,n,M}]^T \in \mathbb{C}^{M \times 1}$ and $\mathbf{x}(t) \triangleq [x_1(t), \dots, x_M(t)]^T \triangleq \mathbf{x}_I(t) + \mathbf{x}_P(t) \in \mathbb{C}^{M \times 1}$, where

$$\mathbf{x}_I(t) = \Re \left\{ \sum_{n=1}^N \mathbf{w}_{I,n} \tilde{x}_{I,n}(t) e^{j2\pi f_n t} \right\}, \quad (2)$$

$$\mathbf{x}_P(t) = \Re \left\{ \sum_{n=1}^N \mathbf{w}_{P,n} e^{j2\pi f_n t} \right\} \quad (3)$$

are the modulated and multisine components, respectively.

B. Reflection Pattern and Composite Channel

According to Green's decomposition [34], the backscattered signal of an antenna can be decomposed into the *structural mode* component and the *antenna mode* component. The former is fixed for a given antenna and can be regarded as part of the environment multipath, while the latter is adjustable and depends on the mismatch of the antenna and load impedances. IRS element $l \in \{1, \dots, L\}$ varies its impedance $Z_l = R_l + jX_l$ in a fully passive manner to reflect the incoming signal, and the reflection coefficient is defined as

$$\phi_l = \frac{Z_l - Z_0}{Z_l + Z_0} \triangleq \eta_l e^{j\theta_l} \quad (4)$$

where Z_0 is the characteristic impedance, $\eta_l \in [0, 1]$ is the reflection amplitude, and $\theta_l \in [0, 2\pi)$ is the phase shift¹. We also define $\mathbf{\Theta} \triangleq \text{diag}(\phi_1, \dots, \phi_L) \in \mathbb{C}^{L \times L}$ as the IRS matrix and let $\boldsymbol{\phi} \triangleq [\phi_1, \dots, \phi_L]^H \in \mathbb{C}^{L \times 1}$ be the IRS vector².

Remark 1. The element impedance Z_l maps to the reflection coefficient ϕ_l uniquely. Since the reactance X_l depends on the frequency, the reflection coefficient ϕ_l is also a function of frequency and cannot be designed independently at different subbands. In this paper, we assume the bandwidth is incomparable to the operating frequency such that the reflection coefficient of each IRS element is the same at all subbands.

Remark 2. The cascaded channel response varies at different frequencies. Since we assume the reflection coefficient to be frequency-flat, there exists a tradeoff for auxiliary channel design in the frequency domain. Moreover, each IRS element simultaneously assists all transmit antennas such that the reflection coefficient is shared by M cascaded channels over N subbands.

At subband n , we denote the AP-UE direct channel as $\mathbf{h}_{D,n}^H \in \mathbb{C}^{1 \times M}$, AP-IRS incident channel as $\mathbf{H}_{I,n} \in \mathbb{C}^{L \times M}$, and IRS-UE reflective channel as $\mathbf{h}_{R,n}^H \in \mathbb{C}^{1 \times L}$. The auxiliary link provided by the IRS can be modeled as a concatenation of the incident channel, the IRS reflection, and the reflective channel. Hence, the composite equivalent channel reduces to

$$\mathbf{h}_n^H = \mathbf{h}_{D,n}^H + \mathbf{h}_{R,n}^H \mathbf{\Theta} \mathbf{H}_{I,n} = \mathbf{h}_{D,n}^H + \boldsymbol{\phi}^H \mathbf{V}_n \quad (5)$$

where we define the cascaded AP-IRS-UE channel (without IRS reflection) as $\mathbf{V}_n \triangleq \text{diag}(\mathbf{h}_{R,n}^H) \mathbf{H}_{I,n} \in \mathbb{C}^{L \times M}$.

¹Due to the non-zero power consumption at the IRS, practically $R_l > 0$ such that $\eta_l < 1$ and depends on θ_l . This paper sticks to the commonest and simplest IRS model where the reflection coefficient is assumed unit.

²Note the conjugate transpose in the notation of $\boldsymbol{\phi}$ makes its entries the complex conjugate of the diagonal entries of $\mathbf{\Theta}$.

C. Received Signal

The total received signal at the single-antenna UE can be decomposed as $y(t) \triangleq y_I(t) + y_P(t)$, where

$$y_I(t) = \Re \left\{ \sum_{n=1}^N \mathbf{h}_n^H \mathbf{w}_{I,n} \tilde{x}_{I,n}(t) e^{j2\pi f_n t} \right\}, \quad (6)$$

$$y_P(t) = \Re \left\{ \sum_{n=1}^N \mathbf{h}_n^H \mathbf{w}_{P,n} e^{j2\pi f_n t} \right\} \quad (7)$$

capture the contribution of modulated and multisine waveforms over all subbands. Note that $y_I(t)$ can also be used for energy harvesting if necessary, but $y_P(t)$ is unmodulated and cannot be used for information decoding.

D. Transceiving Modes

TS and PS are acknowledged as two practical transceiving modes for SWIPT. TS relies on perfect clock synchronization, where the transmitter divides each slot into dedicated data session with length $1-\eta$ and energy session with length η , then designs the waveform for Wireless Information Transfer (WIT) and WPT independently. At the receiver, only information decoder or energy harvester is activated at a time. Varying η from 0 to 1 corresponds to a R-E segment from the WIT point to the WPT point. On the other hand, the PS waveform consists of modulated and multisine components, and the receiver splits the incoming signal into individual data stream with power ratio $1-\rho$ and energy stream with power ratio ρ . Note that in PS the splitting ratio ρ and the superposed waveform require a joint optimization, but in TS the duration ratio η is irrelevant to the waveform design in both sessions. Therefore, we focus on PS in the following context as TS can be regarded as a special case.

E. Information Decoder

A major benefit of the superposed waveform is that the multisine is deterministic and creates no interference to the modulated waveform. Therefore, the achievable rate writes as

$$R(\phi, \mathbf{w}_I, \rho) = \sum_{n=1}^N \log_2 \left(1 + \frac{(1-\rho) |\mathbf{h}_n^H \mathbf{w}_{I,n}|^2}{\sigma_n^2} \right) \quad (8)$$

where σ_n^2 is the variance of the total noise (at RF-band and during RF-to-baseband conversion) on tone n . Rate (8) is achievable with either waveform cancellation or translated demodulation [14].

F. Energy Harvester

In this section, we briefly revisit a tractable nonlinear rectenna model that relates the harvester output DC current to the received signal. Fig. 2a illustrates the equivalent circuit of an ideal antenna, where the antenna has an impedance R_A and the incoming signal creates a voltage source $v_S(t)$. Let R_{in} be the total input impedance of the rectifier and matching network, and we assume the voltage across the matching network is negligible. When perfectly matched ($R_{in} = R_A$), the rectifier input voltage is $v_{in}(t) = y(t) \sqrt{\rho R_A}$.

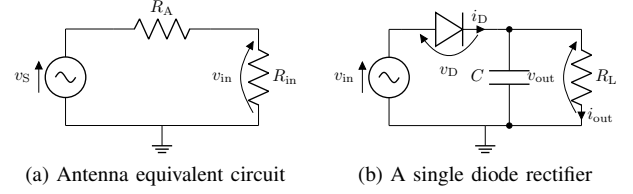


Fig. 2. Receive antenna and energy harvester circuits.

Rectifiers consist of nonlinear components as diode and capacitor to produce DC output and store energy [35]. Consider a simplified rectifier model in Fig. 2b where a single series diode is followed by a low-pass filter with a parallel load. As detailed in [8], [14], a truncated Taylor expansion of the diode I-V characteristic equation suggests that, when the subband frequencies are evenly-spaced, maximizing the average output DC current is equivalent to maximizing a monotonic function ³

$$z(\phi, \mathbf{w}_I, \mathbf{w}_P, \rho) = \sum_{i \text{ even}, i \geq 2}^{n_0} k_i \rho^{i/2} R_A^{i/2} \mathbb{E} \{ \mathbf{A} \{ y(t)^i \} \} \quad (9)$$

where n_0 is the truncation order and $k_i \triangleq i_S / (i! (n' v_T)^i)$ is the diode coefficient (i_S is the reverse bias saturation current, n' is the diode ideality factor, v_T is the thermal voltage). With a slight abuse of notation, we refer to z as the average output DC current in this paper. It can be observed that the traditional linear harvester model, where the output DC power equals the sum of the power harvested on each frequency, is a special case of (9) with $n_0 = 2$. However, due to the coupling effect among different frequencies, some high-order AC components compensate each other and further contribute to the output DC power. In other words, even-order terms with $i \geq 4$ account for the diode nonlinear behavior. For simplicity, we choose $n_0 = 4$ to investigate the fundamental rectifier nonlinearity, and define $\beta_2 \triangleq k_2 R_A$, $\beta_4 \triangleq k_4 R_A^2$ to rewrite z by (10). Note that $\mathbb{E} \{ |\tilde{x}_{I,n}|^2 \} = 1$ but $\mathbb{E} \{ |\tilde{x}_{I,n}|^4 \} = 2$, which applies a modulation gain on the nonlinear terms of the output DC current. Inspired by [36], we further stack $\mathbf{h} \triangleq [\mathbf{h}_1^T, \dots, \mathbf{h}_N^T]^T \in \mathbb{C}^{MN \times 1}$, $\mathbf{w}_{I/P} \triangleq [\mathbf{w}_{I/P,1}^T, \dots, \mathbf{w}_{I/P,N}^T]^T \in \mathbb{C}^{MN \times 1}$, and define $\mathbf{W}_{I/P} \triangleq \mathbf{w}_{I/P} \mathbf{w}_{I/P}^H \in \mathbb{C}^{MN \times MN}$. As illustrated by Fig. 3, $\mathbf{W}_{I/P}$ can be divided into $N \times N$ blocks of size $M \times M$, and we let $\mathbf{W}_{I/P,k}$ keep its block diagonal $k \in \{-N+1, \dots, N-1\}$ and set all other blocks to $\mathbf{0}^{M \times M}$. Hence, the components of z reduce to (11) – (14).

G. Rate-Energy Region

The achievable R-E region is defined as

$$C_{R_{ID}-I_{EH}}(P) \triangleq \left\{ (R_{ID}, I_{EH}) : R_{ID} \leq R, I_{EH} \leq z, \frac{1}{2} (\|\mathbf{w}_I\|^2 + \|\mathbf{w}_P\|^2) \leq P \right\} \quad (15)$$

where P is the average transmit power budget and $1/2$ converts the peak value of sine waves to the average value.

³Note that this small-signal expansion model is only valid for the non-linear operation region of the diode, and the I-V relationship would be linear if the diode behavior is dominated by the load [8].

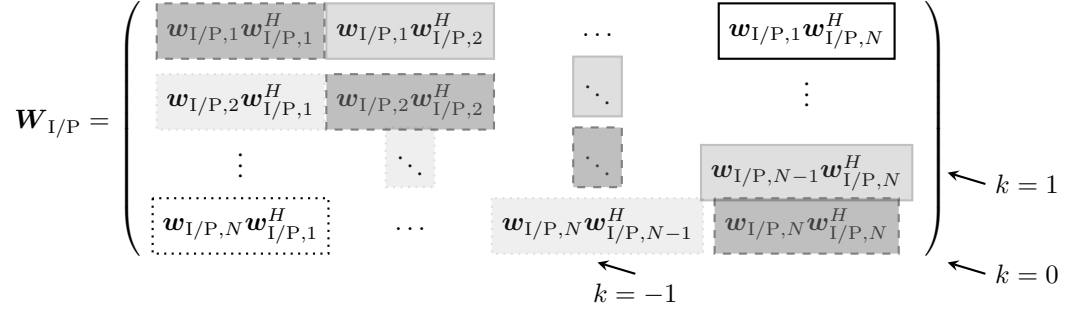


Fig. 3. $\mathbf{W}_{I/P}$ consists of $N \times N$ blocks of size $M \times M$. $\mathbf{W}_{I/P,k}$ keeps the k -th block diagonal of $\mathbf{W}_{I/P}$ and nulls all remaining blocks. Solid, dashed and dotted blocks correspond to $k > 0$, $k = 0$ and $k < 0$, respectively. For $\mathbf{w}_{I/P,n_1} \mathbf{w}_{I/P,n_2}^H$, the k -th block diagonal satisfies $k = n_2 - n_1$.

III. PROBLEM FORMULATION

We characterize each R-E boundary point through a current maximization problem subject to transmit power, IRS magnitude, and rate constraint as

$$\max_{\phi, \mathbf{w}_I, \mathbf{w}_P, \rho} z(\phi, \mathbf{w}_I, \mathbf{w}_P, \rho) \quad (16a)$$

$$\text{s.t.} \quad \frac{1}{2} (\|\mathbf{w}_I\|^2 + \|\mathbf{w}_P\|^2) \leq P, \quad (16b)$$

$$R(\phi, \mathbf{w}_I, \rho) \geq \bar{R}, \quad (16c)$$

$$|\phi_l| = 1, \quad l = 1, \dots, L, \quad (16d)$$

$$0 \leq \rho \leq 1. \quad (16e)$$

Problem (16) is intricate with coupled variables in non-convex expressions (16a), (16c), (16d). To obtain a feasible solution, we propose an BCD algorithm that iteratively updates 1) the IRS phase shift, 2) the active precoder, 3) the waveform amplitude and splitting ratio, until convergence.

A. Passive Beamforming

In this section, we optimize the IRS phase shift ϕ for any given waveform $\mathbf{w}_{I/P}$ and splitting ratio ρ . Note that

$$|\mathbf{h}_n^H \mathbf{w}_{I,n}|^2 = \mathbf{w}_{I,n}^H \mathbf{h}_n \mathbf{h}_n^H \mathbf{w}_{I,n}$$

$$\begin{aligned} &= \mathbf{w}_{I,n}^H (\mathbf{h}_{D,n} + \mathbf{V}_n^H \phi) (\mathbf{h}_{D,n}^H + \phi^H \mathbf{V}_n) \mathbf{w}_{I,n} \\ &= \mathbf{w}_{I,n}^H \mathbf{M}_n^H \Phi \mathbf{M}_n \mathbf{w}_{I,n} \\ &= \text{Tr}(\mathbf{M}_n \mathbf{w}_{I,n} \mathbf{w}_{I,n}^H \mathbf{M}_n^H \Phi) \\ &= \text{Tr}(\mathbf{C}_n \Phi) \end{aligned} \quad (17)$$

where $\mathbf{M}_n \triangleq [\mathbf{V}_n^H, \mathbf{h}_{D,n}]^H \in \mathbb{C}^{(L+1) \times M}$, t' is an auxiliary variable with unit modulus, $\bar{\phi} \triangleq [\phi^H, t']^H \in \mathbb{C}^{(L+1) \times 1}$, $\Phi \triangleq \bar{\phi} \bar{\phi}^H \in \mathbb{C}^{(L+1) \times (L+1)}$, $\mathbf{C}_n \triangleq \mathbf{M}_n \mathbf{w}_{I,n} \mathbf{w}_{I,n}^H \mathbf{M}_n^H \in \mathbb{C}^{(L+1) \times (L+1)}$. On the other hand, we define $t_{I/P,k}$ as

$$\begin{aligned} t_{I/P,k} &\triangleq \mathbf{h}^H \mathbf{W}_{I/P,k} \mathbf{h} \\ &= \text{Tr}(\mathbf{h} \mathbf{h}^H \mathbf{W}_{I/P,k}) \\ &= \text{Tr}((\mathbf{h}_D + \mathbf{V}^H \phi)(\mathbf{h}_D^H + \phi^H \mathbf{V}) \mathbf{W}_{I/P,k}) \\ &= \text{Tr}(\mathbf{M}^H \Phi \mathbf{M} \mathbf{W}_{I/P,k}) \\ &= \text{Tr}(\mathbf{M} \mathbf{W}_{I/P,k} \mathbf{M}^H \Phi) \\ &= \text{Tr}(\mathbf{C}_{I/P,k} \Phi) \end{aligned} \quad (18)$$

where $\mathbf{V} \triangleq [\mathbf{V}_1, \dots, \mathbf{V}_N] \in \mathbb{C}^{L \times MN}$, $\mathbf{M} \triangleq [\mathbf{V}^H, \mathbf{h}_D]^H \in \mathbb{C}^{(L+1) \times MN}$, $\mathbf{C}_{I/P,k} \triangleq \mathbf{M} \mathbf{W}_{I/P,k} \mathbf{M}^H \in \mathbb{C}^{(L+1) \times (L+1)}$. On

$$z(\phi, \mathbf{w}_I, \mathbf{w}_P, \rho) = \beta_2 \rho \left(\mathbb{E} \{ \mathbb{A} \{ y_I^2(t) \} \} + \mathbb{A} \{ y_P^2(t) \} \right) + \beta_4 \rho^2 \left(\mathbb{E} \{ \mathbb{A} \{ y_I^4(t) \} \} + \mathbb{A} \{ y_P^4(t) \} + 6 \mathbb{E} \{ \mathbb{A} \{ y_I^2(t) \} \} \mathbb{A} \{ y_P^2(t) \} \right), \quad (10)$$

$$\mathbb{E} \{ \mathbb{A} \{ y_I^2(t) \} \} = \frac{1}{2} \sum_{n=1}^N (\mathbf{h}_n^H \mathbf{w}_{I,n}) (\mathbf{h}_n^H \mathbf{w}_{I,n})^* = \frac{1}{2} \mathbf{h}^H \mathbf{W}_{I,0} \mathbf{h}, \quad (11)$$

$$\mathbb{E} \{ \mathbb{A} \{ y_I^4(t) \} \} = \frac{3}{4} \left(\sum_{n=1}^N (\mathbf{h}_n^H \mathbf{w}_{I,n}) (\mathbf{h}_n^H \mathbf{w}_{I,n})^* \right)^2 = \frac{3}{4} (\mathbf{h}^H \mathbf{W}_{I,0} \mathbf{h})^2, \quad (12)$$

$$\mathbb{A} \{ y_P^2(t) \} = \frac{1}{2} \sum_{n=1}^N (\mathbf{h}_n^H \mathbf{w}_{P,n}) (\mathbf{h}_n^H \mathbf{w}_{P,n})^* = \frac{1}{2} \mathbf{h}^H \mathbf{W}_{P,0} \mathbf{h}, \quad (13)$$

$$\mathbb{A} \{ y_P^4(t) \} = \frac{3}{8} \sum_{\substack{n_1, n_2, n_3, n_4 \\ n_1 + n_2 = n_3 + n_4}} (\mathbf{h}_{n_1}^H \mathbf{w}_{P,n_1}) (\mathbf{h}_{n_2}^H \mathbf{w}_{P,n_2}) (\mathbf{h}_{n_3}^H \mathbf{w}_{P,n_3})^* (\mathbf{h}_{n_4}^H \mathbf{w}_{P,n_4})^* = \frac{3}{8} \sum_{k=-N+1}^{N-1} (\mathbf{h}^H \mathbf{W}_{P,k} \mathbf{h}) (\mathbf{h}^H \mathbf{W}_{P,k} \mathbf{h})^*. \quad (14)$$

top of this, (8) and (10) reduce to

$$R(\Phi) = \sum_{n=1}^N \log_2 \left(1 + \frac{(1-\rho)\text{Tr}(C_n \Phi)}{\sigma_n^2} \right), \quad (19)$$

$$\begin{aligned} z(\Phi) = & \frac{1}{2}\beta_2\rho(t_{1,0} + t_{P,0}) \\ & + \frac{3}{8}\beta_4\rho^2 \left(2t_{1,0}^2 + \sum_{k=-N+1}^{N-1} t_{P,k}t_{P,k}^* \right) \\ & + \frac{3}{2}\beta_4\rho^2 t_{1,0}t_{P,0}. \end{aligned} \quad (20)$$

To maximize the non-concave expression (20), we propose a SCA algorithm and lower bound the second-order terms by their first-order Taylor expansions [37]. Based on the solution at iteration $i-1$, the approximations at iteration i are

$$(t_{1,0}^{(i)})^2 \geq 2t_{1,0}^{(i)}t_{1,0}^{(i-1)} - (t_{1,0}^{(i-1)})^2, \quad (21)$$

$$t_{P,k}^{(i)}(t_{P,k}^{(i)})^* \geq 2\Re \left\{ t_{P,k}^{(i)}(t_{P,k}^{(i-1)})^* \right\} - t_{P,k}^{(i-1)}(t_{P,k}^{(i-1)})^*, \quad (22)$$

$$\begin{aligned} t_{1,0}^{(i)}t_{P,0}^{(i)} &= \frac{1}{4}(t_{1,0}^{(i)} + t_{P,0}^{(i)})^2 - \frac{1}{4}(t_{1,0}^{(i)} - t_{P,0}^{(i)})^2 \\ &\geq \frac{1}{2}(t_{1,0}^{(i)} + t_{P,0}^{(i)})(t_{1,0}^{(i-1)} + t_{P,0}^{(i-1)}) \\ &\quad - \frac{1}{4}(t_{1,0}^{(i-1)} + t_{P,0}^{(i-1)})^2 - \frac{1}{4}(t_{1,0}^{(i)} - t_{P,0}^{(i)})^2. \end{aligned} \quad (23)$$

Plugging (21) – (23) into (20), we obtain the DC current approximation (24) and transform problem (16) to

$$\max_{\Phi} \quad \tilde{z}(\Phi) \quad (25a)$$

$$\text{s.t.} \quad R(\Phi) \geq \bar{R}, \quad (25b)$$

$$\Phi_{l',l'} = 1, \quad l' = 1, \dots, L+1, \quad (25c)$$

$$\Phi \succeq 0, \quad (25d)$$

$$\text{rank}(\Phi) = 1. \quad (25e)$$

Note that problem (25) is not a Semidefinite Programming (SDP) such that relaxing the rank constraint (25e) has no analytical performance guarantee. In Section IV, we prove through numerical simulations that the solution Φ^* to 25a – 25d is rank-1 under different configurations for all tested channel realizations. It suggests that the rank constraint (25e) can be dropped with negligible loss and $\bar{\Phi}^*$ can be obtained by eigen decomposition. In case Φ^* is not rank-1, a high-quality solution can be extracted via the Gaussian randomization method [38]. Specifically, we decompose $\Phi^* = U\Lambda U^H$, generate CSCG random vector $q \in \{1, \dots, Q\}$ by $\xi_q \sim \mathcal{CN}(\mathbf{0}, \mathbf{I}_{L+1})$, construct the candidate $\bar{\Phi}_q = e^{j \arg(U\Lambda^{1/2}\xi_q)}$, and choose the $\bar{\Phi}^*$ that maximizes (25a) as the solution. Finally, the phase shift of element l is retrieved by $\theta_l^* = \arg(\bar{\Phi}_l^*/\bar{\Phi}_{L+1}^*)$. Problem (25) after rank relaxation can be solved by existing

Algorithm 1 SCA: IRS Phase Shift.

```

1: Input  $\beta_2, \beta_4, \mathbf{h}_{D,n}, \mathbf{V}_n, \mathbf{w}_{I/P,n}, \rho, \sigma_n, \bar{R}, Q, \epsilon, \forall n$ 
2: Construct  $\mathbf{V}, \mathbf{M}, \mathbf{M}_n, \mathbf{C}_n, \mathbf{C}_{I/P,k}, \forall n, k$ 
3: Initialize  $i \leftarrow 0, \Phi^{(0)}$ 
4: Get  $t_{I/P,k}^{(0)}, \forall k$  by (18)
5: Repeat
6:    $i \leftarrow i + 1$ 
7:   Get  $\Phi^{(i)}$  by solving 25a – 25d
8:   Update  $t_{I/P,k}^{(i)}, \forall k$  by (18)
9:   Compute  $z^{(i)}$  by (20)
10: Until  $|z^{(i)} - z^{(i-1)}| \leq \epsilon$ 
11: Set  $\Phi^* = \Phi^{(i)}$ 
12: If  $\text{rank}(\Phi^*) = 1$  Then
13:   Get  $\bar{\Phi}^*$  by eigen decomposition,  $\Phi^* = \bar{\Phi}^*(\bar{\Phi}^*)^H$ 
14: Else
15:   Get  $\mathbf{U}, \mathbf{\Lambda}$  by eigen decomposition,  $\Phi^* = \mathbf{U}\mathbf{\Lambda}\mathbf{U}^H$ 
16:   Generate  $\xi_q \sim \mathcal{CN}(\mathbf{0}, \mathbf{I}_{L+1}), \forall q$ 
17:   Construct  $\bar{\Phi}_q = e^{j \arg(\mathbf{U}\mathbf{\Lambda}^{1/2}\xi_q)}, \bar{\Phi}_q = \bar{\Phi}_q \bar{\Phi}_q^H, \forall q$ 
18:   Set  $q^* = \arg \max_q z(\bar{\Phi}_q), \bar{\Phi}^* = \bar{\Phi}_{q^*}$ 
19: End If
20: Set  $\theta_l^* = \arg(\bar{\Phi}_l^*/\bar{\Phi}_{L+1}^*), \forall l, \Phi^* = [e^{j\theta_1^*}, \dots, e^{j\theta_L^*}]^H$ 
21: Output  $\Phi^*$ 

```

optimization tools such as CVX [39]. The SCA algorithm of passive beamforming is summarized in Algorithm 1.

Proposition 1. *For any feasible initial point, the proposed SCA Algorithm 1 can provide a local optimal Φ^* that satisfies the KKT conditions, although there is no guarantee Φ^* is rank-1.*

Proof. The objective function (25a) is non-decreasing over iterations because the solution of problem (25) at iteration $i-1$ is still a feasible point at iteration i . Moreover, the sequence $\{\tilde{z}(\Phi^{(i)})\}_{i=1}^\infty$ is bounded above due to the unit-modulus constraint (25c). Thus, Algorithm 1 is guaranteed to converge. To prove $\Phi^{(i)}$ converges to stationary points, we notice that the SCA-based Algorithm 1 is indeed an inner approximation algorithm [40], since $\tilde{z}(\Phi) \leq z(\Phi)$, $\partial \tilde{z}(\Phi^{(i)})/\partial \Phi = \partial z(\Phi^{(i)})/\partial \Phi$ and the approximation (21) – (23) are asymptotically tight as $i \rightarrow \infty$ [41]. Therefore, Algorithm 1 is guaranteed to provide a local optimal Φ^* of the original passive beamforming problem (i.e. maximize (20) s.t. (25b) – (25d)) that satisfies the KKT conditions. \square

B. Active Beamforming

In the single-user scenario, the global optimal information and power precoders coincide at MRT. To prove this, we

$$\begin{aligned} \tilde{z}(\Phi^{(i)}) = & \frac{1}{2}\beta_2\rho(t_{1,0}^{(i)} + t_{P,0}^{(i)}) + \frac{3}{8}\beta_4\rho^2 \left(4t_{1,0}^{(i)}t_{1,0}^{(i-1)} - 2(t_{1,0}^{(i-1)})^2 + \sum_{k=-N+1}^{N-1} 2\Re \left\{ t_{P,k}^{(i)}(t_{P,k}^{(i-1)})^* \right\} - t_{P,k}^{(i-1)}(t_{P,k}^{(i-1)})^* \right) \\ & + \frac{3}{2}\beta_4\rho^2 \left(\frac{1}{2}(t_{1,0}^{(i)} + t_{P,0}^{(i)})(t_{1,0}^{(i-1)} + t_{P,0}^{(i-1)}) - \frac{1}{4}(t_{1,0}^{(i-1)} + t_{P,0}^{(i-1)})^2 - \frac{1}{4}(t_{1,0}^{(i)} - t_{P,0}^{(i)})^2 \right). \end{aligned} \quad (24)$$

decouple the waveform in the spatial and frequency domains by

$$\mathbf{w}_{I/P,n} = s_{I/P,n} \mathbf{b}_{I/P,n} \quad (26)$$

where $s_{I/P,n}$ denotes the amplitude of modulated/multisine waveform at tone n , and $\mathbf{b}_{I/P,n}$ denotes the information/power precoder. Define $\mathbf{s}_{I/P} \triangleq [s_{I/P,1}, \dots, s_{I/P,N}]^T \in \mathbb{C}^{N \times 1}$ and $\mathbf{b}_{I/P} \triangleq [\mathbf{b}_{I/P,1}^T, \dots, \mathbf{b}_{I/P,N}^T]^T \in \mathbb{C}^{MN \times 1}$ for simplicity. The MRT precoder at subband n is given by

$$\mathbf{b}_{I/P,n}^* = \frac{\mathbf{h}_n}{\|\mathbf{h}_n\|} \quad (27)$$

From the perspective of WIT, the MRT precoder maximizes $|\mathbf{h}_n^H \mathbf{w}_{I,n}| = \|\mathbf{h}_n\| s_{I,n}$ thus maximizes the rate (8). From the perspective of WPT, the MRT precoder maximizes $(\mathbf{h}_n^H \mathbf{w}_{I/P,n})(\mathbf{h}_n^H \mathbf{w}_{I/P,n})^* = \|\mathbf{h}_n\|^2 s_{I/P,n}^2$ thus maximizes the second and fourth order DC terms (11) – (14). Hence, MRT is the global optimal active precoder and no dedicated energy beams are required in the single-user SWIPT.

C. Waveform and Splitting Ratio

Next, we jointly optimize the waveform amplitude $\mathbf{s}_{I/P}$ and the splitting ratio ρ for any given IRS phase shift ϕ and active precoder $\mathbf{b}_{I/P}$. On top of (27), the equivalent channel strength at subband n is $\|\mathbf{h}_n\|$ and the power allocated to the modulated/multisine waveform is $s_{I/P,n}^2$. Hence, rate (8) reduces to

$$R(\mathbf{s}_I, \rho) = \log_2 \prod_{n=1}^N \left(1 + \frac{(1-\rho)\|\mathbf{h}_n\|^2 s_{I,n}^2}{\sigma_n^2} \right) \quad (28)$$

and DC current (10) reduces to (29), so that problem (16) boils down to

$$\max_{\mathbf{s}_I, \mathbf{s}_P, \rho} z(\mathbf{s}_I, \mathbf{s}_P, \rho) \quad (30a)$$

$$\text{s.t.} \quad \frac{1}{2} (\|\mathbf{s}_I\|^2 + \|\mathbf{s}_P\|^2) \leq P, \quad (30b)$$

$$R(\mathbf{s}_I, \rho) \geq \bar{R}. \quad (30c)$$

Following [14], we introduce auxiliary variables $t'', \bar{\rho}$ and transform it into a reversed GP

$$\min_{\mathbf{s}_I, \mathbf{s}_P, \rho, \bar{\rho}, t''} \frac{1}{t''} \quad (31a)$$

$$\text{s.t.} \quad \frac{1}{2} (\|\mathbf{s}_I\|^2 + \|\mathbf{s}_P\|^2) \leq P, \quad (31b)$$

$$\frac{t''}{z(\mathbf{s}_I, \mathbf{s}_P, \rho)} \leq 1, \quad (31c)$$

$$\frac{2\bar{R}}{\prod_{n=1}^N (1 + \bar{\rho}\|\mathbf{h}_n\|^2 s_{I,n}^2 / \sigma_n^2)} \leq 1, \quad (31d)$$

$$\rho + \bar{\rho} \leq 1. \quad (31e)$$

The denominators of (31c), (31d) are posynomials [42] which can be decomposed as sums of monomials

$$z(\mathbf{s}_I, \mathbf{s}_P, \rho) \triangleq \sum_{m_P} g_{m_P}(\mathbf{s}_I, \mathbf{s}_P, \rho), \quad (32)$$

$$1 + \frac{\bar{\rho}\|\mathbf{h}_n\|^2 s_{I,n}^2}{\sigma_n^2} \triangleq \sum_{m_{I,n}} g_{m_{I,n}}(s_{I,n}, \bar{\rho}) \quad (33)$$

where $m_P = (2N^3 + 6N^2 + 7N)/3$ and $m_{I,n} = 2$. We then upper bound (32) and (33) by Arithmetic Mean-Geometric Mean (AM-GM) inequality [43] and transform problem (31) to

$$\min_{\mathbf{s}_I, \mathbf{s}_P, \rho, \bar{\rho}, t''} \frac{1}{t''} \quad (34a)$$

$$\text{s.t.} \quad \frac{1}{2} (\|\mathbf{s}_I\|^2 + \|\mathbf{s}_P\|^2) \leq P, \quad (34b)$$

$$t'' \prod_{m_P} \left(\frac{g_{m_P}(\mathbf{s}_I, \mathbf{s}_P, \rho)}{\gamma_{m_P}} \right)^{-\gamma_{m_P}} \leq 1, \quad (34c)$$

$$2\bar{R} \prod_n \prod_{m_{I,n}} \left(\frac{g_{m_{I,n}}(s_{I,n}, \bar{\rho})}{\gamma_{m_{I,n}}} \right)^{-\gamma_{m_{I,n}}} \leq 1, \quad (34d)$$

$$\rho + \bar{\rho} \leq 1 \quad (34e)$$

where $\gamma_{m_P}, \gamma_{m_{I,n}} \geq 0$, $\sum_{m_P} \gamma_{m_P} = \sum_{m_{I,n}} \gamma_{m_{I,n}} = 1$. The tightness of the AM-GM inequality depends on $\{\gamma_{m_P}, \gamma_{m_{I,n}}\}$ that require successive update, and a feasible choice at iteration i is

$$\gamma_{m_P}^{(i)} = \frac{g_{m_P}(\mathbf{s}_I^{(i-1)}, \mathbf{s}_P^{(i-1)}, \rho^{(i-1)})}{z(\mathbf{s}_I^{(i-1)}, \mathbf{s}_P^{(i-1)}, \rho^{(i-1)})}, \quad (35)$$

$$\gamma_{m_{I,n}}^{(i)} = \frac{g_{m_{I,n}}(s_{I,n}^{(i-1)}, \bar{\rho}^{(i-1)})}{1 + \bar{\rho}^{(i-1)}\|\mathbf{h}_n\|^2 (s_{I,n}^{(i-1)})^2 / \sigma_n^2}. \quad (36)$$

$\mathbf{s}_I, \mathbf{s}_P, \rho$ are updated iteratively until convergence. Problem (34) can be solved by existing optimization tools such as CVX [39]. The GP algorithm of joint waveform amplitude and splitting ratio optimization is summarized in Algorithm 2.

Proposition 2. *For any feasible initial point, the GP Algorithm 2 is guaranteed to converge to a local optimal point of the waveform amplitude and splitting ratio problem (30).*

Proof. See [8], [14]. \square

$$\begin{aligned} z(\mathbf{s}_I, \mathbf{s}_P, \rho) = & \frac{1}{2} \beta_2 \rho \sum_{n=1}^N \|\mathbf{h}_n\|^2 (s_{I,n}^2 + s_{P,n}^2) + \frac{3}{8} \beta_4 \rho^2 \left(2 \sum_{n_1, n_2} \prod_{j=1}^2 \|\mathbf{h}_{n_j}\|^2 s_{I,n_j}^2 + \sum_{\substack{n_1, n_2, n_3, n_4 \\ n_1 + n_2 = n_3 + n_4}} \prod_{j=1}^4 \|\mathbf{h}_{n_j}\| s_{P,n_j} \right) \\ & + \frac{3}{2} \beta_4 \rho^2 \left(\sum_{n_1, n_2} \|\mathbf{h}_{n_1}\|^2 \|\mathbf{h}_{n_2}\|^2 s_{I,n_1}^2 s_{P,n_2}^2 \right). \end{aligned} \quad (29)$$

Algorithm 2 GP: Waveform Amplitude and Splitting Ratio.

```

1: Input  $\beta_2, \beta_4, \mathbf{h}_n, P, \sigma_n, \bar{R}, \epsilon, \forall n$ 
2: Initialize  $i \leftarrow 0, \mathbf{s}_{I/P}^{(0)}, \rho^{(0)}$ 
3: Repeat
4:    $i \leftarrow i + 1$ 
5:   Update  $\{\gamma_{m_P}^{(i)}, \gamma_{m_{I,n}}^{(i)}\}, \forall n$  by (35), (36)
6:   Get  $\mathbf{s}_{I/P}^{(i)}, \rho^{(i)}$  by solving problem (34)
7:   Compute  $z^{(i)}$  by (29)
8: Until  $|z^{(i)} - z^{(i-1)}| \leq \epsilon$ 
9: Set  $\mathbf{s}_{I/P}^* = \mathbf{s}_{I/P}^{(i)}, \rho^* = \rho^{(i)}$ 
10: Output  $\mathbf{s}_I^*, \mathbf{s}_P^*, \rho^*$ 

```

Algorithm 3 BCD: Waveform, Beamforming and Splitting Ratio.

```

1: Input  $\beta_2, \beta_4, \mathbf{h}_{D,n}, \mathbf{V}_n, P, \sigma_n, \bar{R}, Q, \epsilon, \forall n$ 
2: Initialize  $i \leftarrow 0, \phi^{(0)}, \mathbf{b}_{I/P}^{(0)}, \mathbf{s}_{I/P}^{(0)}, \rho^{(0)}$ 
3: Get  $\mathbf{w}_{I/P,n}^{(0)}, \forall n$  by (26)
4: Repeat
5:    $i \leftarrow i + 1$ 
6:   Get  $\phi^{(i)}$  based on  $\mathbf{w}_{I/P}^{(i-1)}, \rho^{(i-1)}$  by Algorithm 1
7:   Update  $\mathbf{h}_n^{(i)}, \forall n$  by (5)
8:   Get  $\mathbf{s}_{I/P}^{(i)}, \rho^{(i)}$  based on  $\mathbf{h}_n^{(i)}, \forall n$  by Algorithm 2
9:   Update  $\mathbf{w}_{I/P,n}^{(i)}, \forall n$  by (26)
10:  Compute  $z^{(i)}$  by (29)
11: Until  $|z^{(i)} - z^{(i-1)}| \leq \epsilon$ 
12: Set  $\phi^* = \phi^{(i)}, \mathbf{w}_{I/P}^* = \mathbf{w}_{I/P}^{(i)}, \rho^* = \rho^{(i)}$ 
13: Output  $\phi^*, \mathbf{w}_I^*, \mathbf{w}_P^*, \rho^*$ 

```

D. Block Coordinate Descent

Based on the CSIT of direct and cascaded channels, we iteratively update the passive beamforming ϕ by Algorithm 1, the active beamforming $\mathbf{b}_{I/P,n}, \forall n$ by equation (27), and the waveform amplitude $\mathbf{s}_{I/P}$ and splitting ratio ρ by Algorithm 2, until convergence. The BCD algorithm is summarized in Algorithm 3.

Proposition 3. Suppose Φ is rank-1, every limit point $(\phi^*, \mathbf{w}_I^*, \mathbf{w}_P^*, \rho^*)$ provided by the BCD Algorithm 3 is a local optimal point of the original problem (16).

Proof. The objective function (16a) is non-decreasing over iterations of Algorithm 3, which is also upper-bounded due to the unit-modulus constraint (16d) and the transmit power constraint (16b). If Φ is rank-1, then ϕ can be extracted without performance loss and strict convergence of Algorithm 3 is guaranteed. As demonstrated in [44], the limit point obtained by alternatively updating $\phi, \mathbf{b}_{I/P}, \mathbf{s}_{I/P}$ and ρ via BCD is a local optimal solution of problem (16). \square

E. Low-Complexity Adaptive Design

The GP Algorithm 2 achieves local optimality at a cost of exponential computational complexity [43]. To facilitate practical SWIPT implementation, we propose two closed-form adaptive waveform amplitude design by combining WF and SMF under TS and PS setups. The optimal waveform design for

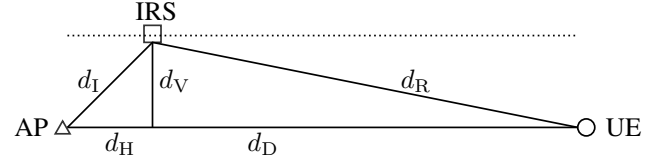


Fig. 4. System layout in simulation.

WIT corresponds to the WF strategy that assigns the amplitude of modulated tone n by

$$s_{I,n} = \sqrt{2 \left(\mu - \frac{\sigma_n^2}{P \|\mathbf{h}_n\|^2} \right)^+} \quad (37)$$

where μ is chosen to satisfy the power constraint $\|\mathbf{s}_I\|^2/2 \leq P$. The closed-form solution can be obtained by iterative power allocation [45] and the details are omitted here. On the other hand, SMF was proposed in [12] as a suboptimal WPT resource allocation scheme that assigns the amplitude of sinewave n by

$$s_{P,n} = \sqrt{\frac{2P}{\sum_{n=1}^N \|\mathbf{h}_n\|^{2\alpha}}} \|\mathbf{h}_n\|^\alpha \quad (38)$$

where the scaling ratio $\alpha \geq 1$ scales the matched filter to exploit the rectifier nonlinearity. In the low-complexity TS waveform design, modulated waveform (37) is used in the data session while multisine waveform (38) is used in the energy session. In contrast, the low-complexity PS scheme jointly designs the waveform balancing ratio δ and splitting ratio ρ , and the amplitude of modulated and multisine components are given by

$$s_{I,n} = \sqrt{2(1-\delta) \left(\mu - \frac{\sigma_n^2}{P \|\mathbf{h}_n\|^2} \right)^+} \quad (39)$$

$$s_{P,n} = \sqrt{\frac{2\delta P}{\sum_{n=1}^N \|\mathbf{h}_n\|^{2\alpha}}} \|\mathbf{h}_n\|^\alpha \quad (40)$$

Besides, minor modifications are required for passive beamforming to cooperate with the low-complexity waveform schemes. To achieve the WIT point ($\eta = \rho = 0$), the achievable rate (19) instead of the DC current (24) should be maximized. To achieve non-WIT points, the rate constraint (25b) should be dropped as the R-E region is now characterized by varying either η or δ, ρ . Algorithm 4 summarizes the modified passive beamforming design under low-complexity PS setup.

Similar to Algorithm 3, we propose a Low-Complexity-BCD (LC-BCD) algorithm that iteratively update the passive beamforming ϕ by Algorithm 4, the active beamforming $\mathbf{b}_{I/P,n}, \forall n$ by equation (27), and the waveform amplitude $\mathbf{s}_{I/P}$ by (37), (38) for TS or (39), (40) for PS, until convergence. Similar to Proposition 3, strict convergence of the LC-BCD algorithm is guaranteed if Φ is rank-1, and the details are omitted here for simplicity.

IV. PERFORMANCE EVALUATIONS

To evaluate the performance of the proposed IRS-aided SWIPT system, we consider the layout in Fig. 4 where the IRS moves along a horizontal line parallel to the AP-UE path. Let d_H, d_V be the horizontal and vertical distances from the

TABLE I

THE MAXIMUM VALUE OF $1 - \nu$ OVER ALL R-E SAMPLES DURING BCD AND LC-BCD ALGORITHMS FOR ALL TESTED CHANNEL REALIZATIONS

| | | M | | | N | | | L | | | B | |
|--|-----|--------|--------|--------|--------|--------|--------|--------|--------|--------|--------|--------|
| $\max(1 - \nu)$ [$\times 10^{-16}$] | BCD | 5.5511 | 6.6613 | 6.6613 | 5.5511 | 6.6613 | 5.5511 | 6.6613 | 5.5511 | 6.6613 | 6.6613 | 5.5511 |
| | LC | 6.6613 | 6.6613 | 6.6613 | 5.5511 | 6.6613 | 5.5511 | 6.6613 | 8.8818 | 6.6613 | 6.6613 | 5.5511 |

Algorithm 4 Modified: IRS Phase Shift.

```

1: Input  $\beta_2, \beta_4, \mathbf{h}_{D,n}, \mathbf{V}_n, \mathbf{w}_{I/P,n}, \rho, \sigma_n, Q, \epsilon, \forall n$ 
2: Construct  $\mathbf{V}, \mathbf{M}, \mathbf{M}_n, \mathbf{C}_n, \mathbf{C}_{I/P,k}, \forall n, k$ 
3: Initialize  $i \leftarrow 0, \Phi^{(0)}$ 
4: If  $\rho = 0$  Then
5:   Get  $\Phi^*$  by maximizing (19) s.t. (25c), (25d)
6: Else
7:   Repeat
8:      $i \leftarrow i + 1$ 
9:     Set  $\bar{R} = 0$ 
10:    Get  $\Phi^{(i)}$  by solving 25a – 25d
11:    Update  $t_{I/P,k}^{(i)}, \forall k$  by (18)
12:    Compute  $z^{(i)}$  by (20)
13:  Until  $|z^{(i)} - z^{(i-1)}| \leq \epsilon$ 
14:  Set  $\Phi^* = \Phi^{(i)}$ 
15: End If
16: If  $\text{rank}(\Phi^*) = 1$  Then
17:   Get  $\bar{\phi}^*$  by eigen decomposition,  $\Phi^* = \bar{\phi}^* (\bar{\phi}^*)^H$ 
18: Else
19:   Get  $\mathbf{U}, \mathbf{\Lambda}$  by eigen decomposition,  $\Phi^* = \mathbf{U} \mathbf{\Lambda} \mathbf{U}^H$ 
20:   Generate  $\xi_q \sim \mathcal{CN}(\mathbf{0}, \mathbf{I}_{L+1}), \forall q$ 
21:   Construct  $\bar{\phi}_q = e^{j \arg(\mathbf{U} \mathbf{\Lambda}^{1/2} \xi_q)}, \Phi_q = \bar{\phi}_q \bar{\phi}_q^H, \forall q$ 
22:   Set  $q^* = \arg \max_q R(\Phi_q)$  or  $q^* = \arg \max_q z(\Phi_q)$ ,
      $\bar{\phi}^* = \bar{\phi}_{q^*}$ 
23: End If
24: Set  $\theta_l^* = \arg(\bar{\phi}_l^* / \bar{\phi}_{L+1}^*), \forall l, \phi^* = [e^{j\theta_1^*}, \dots, e^{j\theta_L^*}]^H$ 
25: Output  $\phi^*$ 

```

AP to the IRS, and denote respectively $d_D, d_I = \sqrt{d_H^2 + d_V^2}$, $d_R = \sqrt{(d_D - d_H)^2 + d_V^2}$ as the distance of direct, incident and reflective links. Consider a large open space Wi-Fi-like environment at center frequency 5.18 GHz, where the fading parameters follow IEEE TGN channel model D [46] and the reference path loss is -35 dB at 1 m. Denote $\Lambda_D, \Lambda_I, \Lambda_R$ as the path loss of direct, incident and reflective links. All channels are assumed NLoS with taps modelled as i.i.d. CSCG random variables of unit average sum-power, corresponding to a normalized multipath response. Rectenna parameters are chosen as $k_2 = 0.0034, k_4 = 0.3829, R_A = 50 \Omega$ such that $\beta_2 = 0.17$ and $\beta_4 = 957.25$. The average Effective Isotropic Radiated Power (EIRP) is fixed to $P = 36$ dBm and the receive antenna gain is set to 2 dBi. For the algorithms, the number of candidates for Gaussian randomization is $Q = 10^3$, the scaling ratio is $\alpha = 2$, the tolerance is $\epsilon = 10^{-8}$, and we assume $\delta = \rho$ for simplicity. Each R-E region is averaged over 300 channel realizations, and the x -axis is normalized to per-subband rate R/N .

We first provide numerical proof on the strict convergence of both BCD algorithms. To see this, we define the eigen

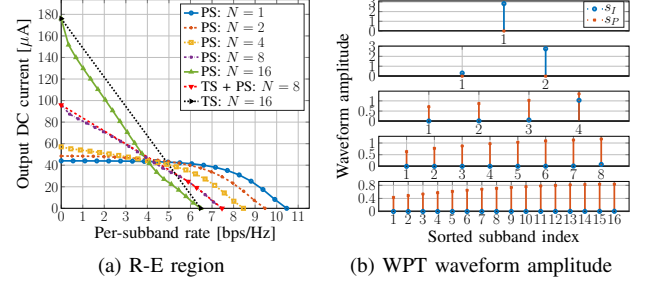


Fig. 5. Average R-E region and WPT waveform amplitude versus N for $M = 1, L = 20, \sigma_n^2 = -40$ dBm, $B = 1$ MHz and $d_H = d_V = 2$ m.

ratio as $\nu = \max_l \lambda_l(\Phi) / \sum_l \lambda_l(\Phi)$ where $\lambda_l(\Phi)$ is the l -th eigenvalue of Φ . Since $\nu = 1$ means Φ is rank-1, we claim Φ is approximately rank-1 when $1 - \nu \approx 0$. Table I shows the maximum value of $1 - \nu$ over 20 R-E samples of 300 tested channel realizations for both BCD algorithms. With reasonable precision, we conclude that Φ is always rank-1 under different configurations for all tested channel realizations. It suggests that the rank constraint 25e can be relaxed with negligible performance loss, ϕ can be directly obtained through eigen decomposition, and the assumption of Proposition 3 always hold such that the BCD Algorithm 3 converges to local optimal points.

Fig. 5a illustrates the average R-E region versus the number of subband N . *First*, it is observed that increasing N reduces the per-subband rate R/N but boosts the harvested energy. It is because less power is given to each subband but more balanced DC terms are introduced to boost the harvested energy. On the other hand, Fig. 5b sorts the modulated/multisine amplitude $s_{I/P}$ for WPT in descending order. It demonstrated that a dedicated multisine waveform is unnecessary for a small N but is required for a large N . This observation originates from the rectifier nonlinearity. Although both waveforms have equivalent second-order DC terms (11) and (13), for the fourth-order terms (12) and (14), the modulated waveform has N^2 monomials with a modulation gain of 2 while the multisine has $(2N^3 + N)/3$ monomials. Hence, the benefit of multisine outstands for a sufficiently large N . *Second*, the R-E region is convex for $N = 2, 4$ and concave-convex for $N = 8, 16$. This has the consequence that PS outperforms TS for a small N and is outperformed for a large N . When N is in between, the optimal strategy is a combination of both, i.e. a time sharing between the WPT point and the saddle SWIPT point obtained by PS (as the red curve in Fig. 5a). Compared with the linear harvester model that requires no dedicated power waveform and always prefer PS, the rectifier nonlinearity enlarges the R-E region by favoring a different waveform and transceiving mode, both heavily depends on the number of subbands.

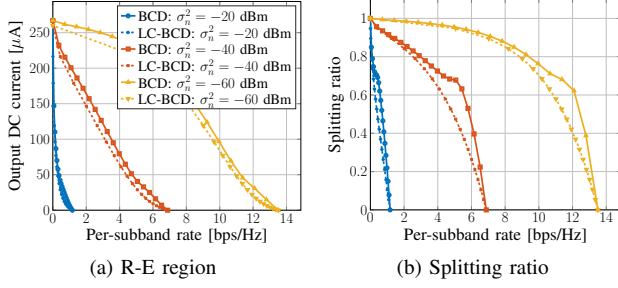


Fig. 6. Average R-E region and Splitting ratio versus σ_n^2 for $M = 1$, $N = 16$, $L = 20$, $B = 1$ MHz and $d_H = d_V = 2$ m.

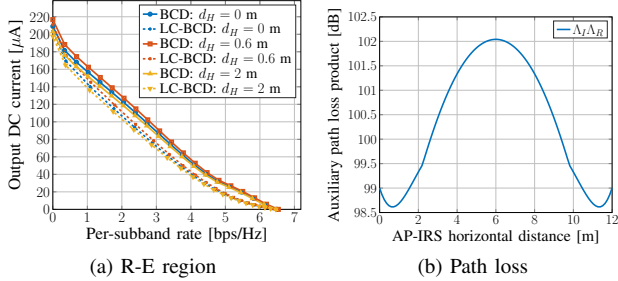


Fig. 7. Average R-E region and path loss versus d_H for $M = 1$, $N = 16$, $L = 20$, $\sigma_n^2 = -40$ dBm, $B = 1$ MHz and $d_V = 2$ m.

The average noise power influences the R-E region as in Fig. 6a. *First*, we note that the R-E region is roughly concave/convex at low/high SNR such that TS/PS are preferred correspondingly. At low SNR, the power is allocated to the modulated waveform on few strongest subbands to achieve a high rate. As the rate constraint \bar{R} decreases, Algorithm 2 activates more subbands that further boosts the harvested DC power due to frequency coupling and harvester nonlinearity. *Second*, there exists a turning point in the R-E region especially for a low noise level ($\sigma_n^2 \leq -40$ dBm). The reason is that when \bar{R} departs slightly from the maximum value, the algorithm tends to adjust the splitting ratio ρ rather than allocating more power to the multisine waveform, since a small-amplitude multisine could be inefficient for energy purpose. As \bar{R} further decreases, due to the advantage of multisine, a modulated waveform with a very large ρ could be outperformed by a superposed waveform with a smaller ρ . The result proves the benefit of superposed waveform and the necessity of joint waveform and splitting ratio optimization.

In Fig. 7a, we compare the average R-E region achieved by different AP-IRS horizontal distance d_H . Different from the active Amplify-and-Forward (AF) relay that favors midpoint development [47], the IRS should be placed close to either the AP or the UE based on the product path loss model that applies to finite-size element reflection [48], [49]. Moreover, there exist two optimal IRS coordinates around $d_H = 0.6$ and 11.4 m that minimize the path loss product $\Lambda_I \Lambda_R$ and maximize the R-E tradeoff. It suggests that equipping the AP with an IRS can potentially extend the operation range of SWIPT systems. Considering the passive characteristic of the IRS, chances are that it can be directly supported by the SWIPT network.

The impacts of the number of transmit antennas M and IRS

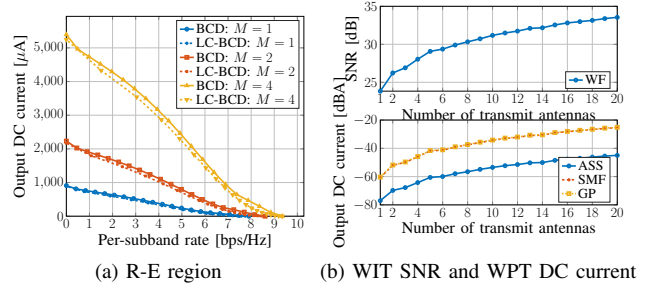


Fig. 8. Average R-E region, WIT SNR and WPT DC current versus M for $N = 16$, $L = 20$, $\sigma_n^2 = -40$ dBm, $B = 1$ MHz, $d_H = d_V = 0.5$ m.

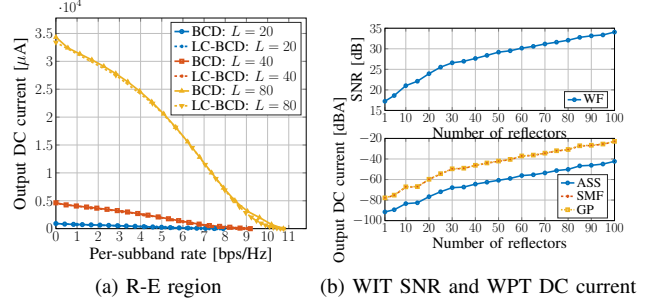


Fig. 9. Average R-E region, WIT SNR and WPT DC current versus L for $M = 1$, $N = 16$, $\sigma_n^2 = -40$ dBm, $B = 1$ MHz and $d_H = d_V = 0.5$ m.

elements L on the R-E behavior are revealed in Fig. 8a and 9a. *First*, adding either active or passive elements enhances the equivalent channel strength to boost information and power transfer. Interestingly, it has negligible influence on the optimal transceiving strategy because both rate and current are proportionally amplified to preserve the general trend of the R-E boundary. *Second*, passive beamforming has a larger array gain and power scaling order than active beamforming. This behavior is more obvious in Fig. 8b and 9b for the case of WIT and WPT, where the Adaptive Single Sinewave (ASS) allocates all power to the sine wave at the strongest subband and is optimal for WPT with linear harvester model [8]. For active beamforming, doubling M brings a 3 dB gain at the output SNR that corresponds to a transmit array gain of M and a doubled harvester input power. Thanks to the rectenna nonlinearity, the output DC current ends up with a nearly four-time (12 dB) increase that validates the active scaling law in the order of M^2 [8]. On the other hand, when the IRS is very close to the AP, doubling L increases the output SNR up to 6 dB that implies a reflect array gain of L^2 . An interpretation is that the IRS coherently combines the incoming signal with a receive array gain L , then performs an equal gain reflection with a transmit array gain L . Hence, doubling IRS elements brings a four-fold increase on the received signal power that further amplifies the harvested DC current by 16 times (24 dB), corresponding to a passive scaling law in the order of L^4 . Compared with active antennas, the IRS achieves higher array gain and power scaling order using passive elements with frequency-dependent reflection, but a very large L is required to compensate the double fading of the auxiliary link. Moreover, the ASS strategy exploit

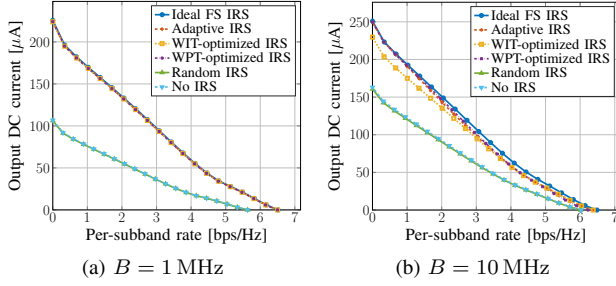


Fig. 10. Average R-E region for ideal, adaptive, fixed and no IRS versus B for $M = 1$, $N = 16$, $L = 20$, $\sigma_n^2 = -40$ dBm and $d_H = d_V = 2$ m.

no harvester nonlinearity and ends up with a nearly 20 dB current gap with SMF and GP. These observations demonstrate the R-E benefit of passive beamforming and emphasize the importance of accounting the harvester nonlinearity in the passive beamforming design.

Fig. 10a and 10b explore the R-E region with different IRS strategies for narrowband and broadband SWIPT. The ideal Frequency-Selective (FS) IRS assumes the reflection coefficient of each element is independent and controllable at different frequencies. The adaptive IRS adjusts the passive beamforming for different rate constraints by Algorithm 1. The WIT/WPT-optimized IRS is retrieved by Algorithm 4 then fixed for the whole R-E region (i.e. the boundary is obtained by varying the waveform amplitude and splitting ratio). *First*, random IRS and no IRS perform worse than other schemes since no passive beamforming is exploited. Their achievable R-E regions coincide because the antenna mode reflection of the random IRS is cancelled out after averaging over channel realizations. *Second*, the performance of non-random IRS are similar when the bandwidth is small, while the adaptive IRS outperforms the WIT/WPT-optimized IRS but is worse than the ideal FS IRS when the bandwidth is large. In the former case, the subband responses are close to each other such that the tradeoff in Remark 2 becomes insignificant and the auxiliary channels can be roughly maximized at all subbands. It suggests that for narrowband SWIPT, the optimal passive beamforming of any R-E point is roughly optimal for the whole R-E region, which can be approximated in the closed form (by aligning the auxiliary channel with the direct channel) when a single transmit antenna is used at the AP. On the other hand, the optimal reflection coefficient varies at different R-E points for broadband SWIPT, since the information and power transfer prefer different channel strength distribution in the frequency domain. By adaptive passive beamforming, the channel strength can be either amplified at few strongest subbands to enhance the rate at low SNR, or spread evenly to boost the output DC power. It shows the R-E advantage of adaptive passive beamforming Algorithm 1 for broadband SWIPT.

We then explore the impact of imperfect cascaded CSIT and quantized IRS on the R-E performance. Due to the general lack of RF-chains at the IRS, it can be challenging to acquire accurate cascaded CSIT on a short-term basis. Consider an imperfect CSIT model where the estimation of the cascaded

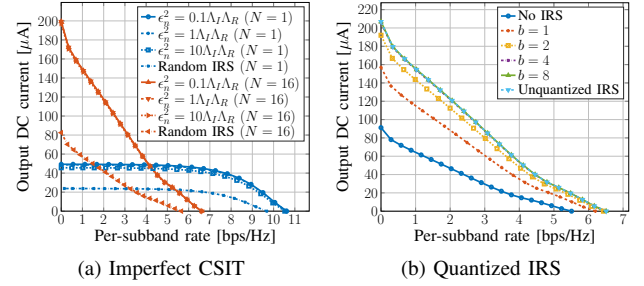


Fig. 11. Average R-E region with imperfect cascaded CSIT and quantized IRS for $M = 1$, $N = 16$, $L = 20$, $\sigma_n^2 = -40$ dBm, $B = 10$ MHz and $d_H = d_V = 2$ m.

link at subband n is

$$\hat{\mathbf{V}}_n = \mathbf{V}_n + \tilde{\mathbf{V}}_n \quad (41)$$

where $\tilde{\mathbf{V}}_n$ is the estimation error with entries following i.i.d. CSCG distribution $\mathcal{CN}(0, \epsilon_n^2)$. Perfect CSIT can be regarded as a special case with $\epsilon_n = 0$. Note that the estimation at different subbands are independent but the subchannel responses are correlated. Figure 11a shows that the proposed passive beamforming Algorithm 1 is robust to cascaded CSIT inaccuracy for broadband SWIPT with different L . On the other hand, since the practical reflection coefficient depends on the element impedance set, we quantize each reflection coefficient by b bits and introduce a passive beamforming codebook $\mathcal{C}_b = \{e^{j2\pi i/2^b} \mid i = 1, \dots, 2^b\}$ to reduce the circuit complexity and control overhead. Figure 11b suggests that even $b = 1$ (i.e. two-state reflection) brings considerable R-E gain over the benchmark scheme without IRS, and the performance gap between $b = 4$ and unquantized IRS is negligible. These observations demonstrate the advantage of the proposed joint waveform, active and passive beamforming design in practical IRS-aided SWIPT systems.

V. CONCLUSION AND FUTURE WORKS

This paper investigated the single-user R-E tradeoff in a novel IRS-aided multi-carrier MISO SWIPT system. Uniquely, we consider the joint waveform, active and passive beamforming design under rectifier nonlinearity and practical transceiving strategies to maximize the achievable R-E region. A three-stage BCD algorithm is proposed to solve the problem. In the first stage, the IRS phase shift is obtained by combining the SCA technique with an relax-then-extract step. In the second and third stages, the active precoder is derived in the closed form and the waveform amplitude is optimized by the reversed GP method. We also propose and combine closed-form adaptive waveform schemes with a modified passive beamforming strategy to formulate a low-complexity BCD algorithm with near-optimal performance. Numerical results prove the convergence of both BCD algorithms and reveal significant R-E gains by accounting harvester nonlinearity in the passive beamforming design. Compared with active antennas, IRS elements are limited to frequency-dependent reflection but are able to integrate coherent combining and equal gain transmission in a fully passive manner to further boost the

array gain and power scaling order. However, a large number of reflecting elements may be required to compensate the double fading in the auxiliary link.

One particular unanswered question of this paper is how to design waveform, active and passive beamforming in a multi-user multi-carrier IRS-aided SWIPT system.

REFERENCES

- [1] B. Clerckx, R. Zhang, R. Schober, D. W. K. Ng, D. I. Kim, and H. V. Poor, "Fundamentals of wireless information and power transfer: From RF energy harvester models to signal and system designs," *IEEE Journal on Selected Areas in Communications*, vol. 37, no. 1, pp. 4–33, 2019.
- [2] L. R. Varshney, "Transporting information and energy simultaneously," *IEEE International Symposium on Information Theory - Proceedings*, pp. 1612–1616, 2008.
- [3] X. Zhou, R. Zhang, and C. K. Ho, "Wireless information and power transfer: Architecture design and rate-energy tradeoff," *IEEE Transactions on Communications*, vol. 61, no. 11, pp. 4754–4767, 2013.
- [4] R. Zhang and C. K. Ho, "MIMO broadcasting for simultaneous wireless information and power transfer," *IEEE Transactions on Wireless Communications*, vol. 12, no. 5, pp. 1989–2001, 2013.
- [5] J. Park and B. Clerckx, "Joint wireless information and energy transfer in a K-user MIMO interference channel," *IEEE Transactions on Wireless Communications*, vol. 13, no. 10, pp. 5781–5796, 2014.
- [6] M. S. Trotter, J. D. Griffin, and G. D. Durgin, "Power-optimized waveforms for improving the range and reliability of RFID systems," *2009 IEEE International Conference on RFID, RFID 2009*, pp. 80–87, 2009.
- [7] B. Clerckx and J. Kim, "On the Beneficial Roles of Fading and Transmit Diversity in Wireless Power Transfer with Nonlinear Energy Harvesting," *IEEE Transactions on Wireless Communications*, vol. 17, no. 11, pp. 7731–7743, 2018.
- [8] B. Clerckx and E. Bayguzina, "Waveform Design for Wireless Power Transfer," *IEEE Transactions on Signal Processing*, vol. 64, no. 23, pp. 6313–6328, 2016.
- [9] J. Kim, B. Clerckx, and P. D. Mitcheson, "Experimental Analysis of Harvested Energy and Throughput Trade-off in a Realistic SWIPT System," in *2019 IEEE Wireless Power Transfer Conference (WPTC)*. IEEE, jun 2019, pp. 1–5.
- [10] —, "Signal and System Design for Wireless Power Transfer : Prototype, Experiment and Validation," *IEEE Transactions on Wireless Communications*, vol. 1276, no. c, pp. 1–1, 2020.
- [11] J. Kim and B. Clerckx, "Range Expansion for Wireless Power Transfer: A Joint Beamforming and Waveform Architecture," *arXiv preprint arXiv:2010.01680*, oct 2020.
- [12] B. Clerckx and E. Bayguzina, "Low-Complexity Adaptive Multisine Waveform Design for Wireless Power Transfer," *IEEE Antennas and Wireless Propagation Letters*, vol. 16, no. 1, pp. 2207–2210, 2017.
- [13] J. Kim, B. Clerckx, and P. D. Mitcheson, "Prototyping and experimentation of a closed-loop wireless power transmission with channel acquisition and waveform optimization," *WPTC 2017 - Wireless Power Transfer Conference*, pp. 1–4, 2017.
- [14] B. Clerckx, "Wireless Information and Power Transfer: Nonlinearity, Waveform Design, and Rate-Energy Tradeoff," *IEEE Transactions on Signal Processing*, vol. 66, no. 4, pp. 847–862, 2018.
- [15] M. Varasteh, B. Rassouli, and B. Clerckx, "On Capacity-Achieving Distributions for Complex AWGN Channels Under Nonlinear Power Constraints and Their Applications to SWIPT," *IEEE Transactions on Information Theory*, vol. 66, no. 10, pp. 6488–6508, 2020.
- [16] —, "SWIPT Signaling over Frequency-Selective Channels with a Nonlinear Energy Harvester: Non-Zero Mean and Asymmetric Inputs," *IEEE Transactions on Communications*, vol. 67, no. 10, pp. 7195–7210, 2019.
- [17] M. Varasteh, J. Hoydis, and B. Clerckx, "Learning to Communicate and Energize: Modulation, Coding and Multiple Access Designs for Wireless Information-Power Transmission," *IEEE Transactions on Communications*, vol. 6778, no. DL, pp. 1–1, 2020.
- [18] R. S. Anwar, L. Mao, and H. Ning, "Frequency selective surfaces: A review," *Applied Sciences (Switzerland)*, vol. 8, no. 9, pp. 1–47, 2018.
- [19] T. J. Cui, M. Q. Qi, X. Wan, J. Zhao, and Q. Cheng, "Coding metamaterials, digital metamaterials and programmable metamaterials," *Light: Science & Applications*, vol. 3, no. 10, pp. e218–e218, 2014.
- [20] C. Liaskos, S. Nie, A. Tsioliaridou, A. Pitsillides, S. Ioannidis, and I. Akyildiz, "Realizing Wireless Communication Through Software-Defined HyperSurface Environments," *19th IEEE International Symposium on a World of Wireless, Mobile and Multimedia Networks, WoWMoM 2018*, 2018.
- [21] Q. Wu and R. Zhang, "Intelligent Reflecting Surface Enhanced Wireless Network: Joint Active and Passive Beamforming Design," in *2018 IEEE Global Communications Conference (GLOBECOM)*, vol. 18, no. 11. IEEE, dec 2018, pp. 1–6.
- [22] —, "Beamforming Optimization for Intelligent Reflecting Surface with Discrete Phase Shifts," in *ICASSP 2019 - 2019 IEEE International Conference on Acoustics, Speech and Signal Processing (ICASSP)*. IEEE, may 2019, pp. 7830–7833.
- [23] —, "Intelligent Reflecting Surface Enhanced Wireless Network via Joint Active and Passive Beamforming," *IEEE Transactions on Wireless Communications*, vol. 18, no. 11, pp. 5394–5409, nov 2019.
- [24] S. Abeywickrama, R. Zhang, and C. Yuen, "Intelligent Reflecting Surface: Practical Phase Shift Model and Beamforming Optimization," in *ICC 2020 - 2020 IEEE International Conference on Communications (ICC)*. IEEE, jun 2020, pp. 1–6.
- [25] Q.-U.-A. Nadeem, A. Kammoun, A. Chaaban, M. Debbah, and M.-S. Alouini, "Intelligent Reflecting Surface Assisted Wireless Communication: Modeling and Channel Estimation," *arXiv preprint arXiv:1906.02360*, pp. 1–7, 2019.
- [26] C. You, B. Zheng, and R. Zhang, "Intelligent Reflecting Surface with Discrete Phase Shifts: Channel Estimation and Passive Beamforming," in *ICC 2020 - 2020 IEEE International Conference on Communications (ICC)*. IEEE, jun 2020, pp. 1–6.
- [27] J.-M. Kang, "Intelligent Reflecting Surface: Joint Optimal Training Sequence and Reflection Pattern," *IEEE Communications Letters*, vol. 24, no. 8, pp. 1784–1788, aug 2020.
- [28] P. Wang, J. Fang, H. Duan, and H. Li, "Compressed Channel Estimation for Intelligent Reflecting Surface-Assisted Millimeter Wave Systems," *IEEE Signal Processing Letters*, vol. 27, pp. 905–909, 2020.
- [29] Y. Yang, S. Zhang, and R. Zhang, "IRS-Enhanced OFDMA: Joint Resource Allocation and Passive Beamforming Optimization," *IEEE Wireless Communications Letters*, pp. 1–1, 2020.
- [30] L. Dai, M. D. Renzo, C. B. Chae, L. Hanzo, B. Wang, M. Wang, X. Yang, J. Tan, S. Bi, S. Xu, F. Yang, and Z. Chen, "Reconfigurable Intelligent Surface-Based Wireless Communications: Antenna Design, Prototyping, and Experimental Results," *IEEE Access*, vol. 8, pp. 45 913–45 923, 2020.
- [31] Q. Wu and R. Zhang, "Weighted Sum Power Maximization for Intelligent Reflecting Surface Aided SWIPT," *IEEE Wireless Communications Letters*, vol. 9, no. 5, pp. 586–590, 2020.
- [32] Y. Tang, G. Ma, H. Xie, J. Xu, and X. Han, "Joint Transmit and Reflective Beamforming Design for IRS-Assisted Multiuser MISO SWIPT Systems," in *ICC 2020 - 2020 IEEE International Conference on Communications (ICC)*. IEEE, jun 2020, pp. 1–6.
- [33] Q. Wu and R. Zhang, "Joint Active and Passive Beamforming Optimization for Intelligent Reflecting Surface Assisted SWIPT Under QoS Constraints," *IEEE Journal on Selected Areas in Communications*, vol. 38, no. 8, pp. 1735–1748, aug 2020.
- [34] R. C. Hansen, "Relationships Between Antennas as Scatterers and as Radiators," *Proceedings of the IEEE*, vol. 77, no. 5, pp. 659–662, 1989.
- [35] M. Piñuela, P. D. Mitcheson, and S. Lucyszyn, "Ambient RF energy harvesting in urban and semi-urban environments," *IEEE Transactions on Microwave Theory and Techniques*, vol. 61, no. 7, pp. 2715–2726, 2013.
- [36] Y. Huang and B. Clerckx, "Large-Scale Multiantenna Multisine Wireless Power Transfer," *IEEE Transactions on Signal Processing*, vol. 65, no. 21, pp. 5812–5827, 2017.
- [37] T. Adali and S. Haykin, *Adaptive Signal Processing*. Hoboken, NJ, USA: John Wiley & Sons, Inc., mar 2010.
- [38] Z.-q. Luo, A. M.-c. So, Y. Ye, and S. Zhang, "Semidefinite Relaxation of Quadratic Optimization Problems -From its practical deployments and scope of applicability to key theoretical results-," *IEEE Signal Processing Magazine*, no. May, pp. 20–34, 2010.
- [39] M. C. Grant and S. P. Boyd, "CVX: Matlab software for disciplined convex programming, version 2.0 beta," 2013. [Online]. Available: <http://cvxr.com/cvx/>
- [40] B. R. Marks and G. P. Wright, "A General Inner Approximation Algorithm for Nonconvex Mathematical Programs," *Operations Research*, vol. 26, no. 4, pp. 681–683, 1978.
- [41] W. C. Li, T. H. Chang, C. Lin, and C. Y. Chi, "Coordinated beamforming for multiuser MISO interference channel under rate outage constraints," *IEEE Transactions on Signal Processing*, vol. 61, no. 5, pp. 1087–1103, 2013.

- [42] S. Boyd, S. J. Kim, L. Vandenberghe, and A. Hassibi, "A tutorial on geometric programming," *Optimization and Engineering*, vol. 8, no. 1, pp. 67–127, 2007.
- [43] M. Chiang, *Geometric Programming for Communication Systems*. now Publishers Inc, 2005, vol. 2, no. 1.
- [44] L. Grippo and M. Sciandrone, "On the convergence of the block nonlinear Gauss-Seidel method under convex constraints," *Operations Research Letters*, vol. 26, no. 3, pp. 127–136, 2000.
- [45] D. Tse and V. Pramod, "Fundamentals of wireless communication," *Fundamentals of Wireless Communication*, vol. 9780521845, pp. 1–564, 2005.
- [46] V. Erceg, "TGn Channel Models," in *IEEE 802.11-03/940r4*, 2004.
- [47] S. Li, K. Yang, M. Zhou, J. Wu, L. Song, Y. Li, and H. Li, "Full-Duplex Amplify-and-Forward Relaying: Power and Location Optimization," *IEEE Transactions on Vehicular Technology*, vol. 66, no. 9, pp. 8458–8468, 2017.
- [48] O. Ozdogan, E. Bjornson, and E. G. Larsson, "Intelligent Reflecting Surfaces: Physics, Propagation, and Pathloss Modeling," *IEEE Wireless Communications Letters*, vol. 9, no. 5, pp. 581–585, 2020.
- [49] W. Tang, M. Z. Chen, X. Chen, J. Y. Dai, Y. Han, M. Di Renzo, Y. Zeng, S. Jin, Q. Cheng, and T. J. Cui, "Wireless Communications With Reconfigurable Intelligent Surface: Path Loss Modeling and Experimental Measurement," *IEEE Transactions on Wireless Communications*, vol. 20, no. 1, pp. 421–439, jan 2021.